High Linearity, Low Hysteresis $Ti_3C_2T_x$ MXene/AgNW/Liquid Metal Self-Healing Strain Sensor Modulated by Dynamic Disulfide and Hydrogen Bonds

Yanli Wang, Wenjing Qin, Min Yang, Zhenhao Tian, Wenjin Guo, Jinkun Sun, Xiang Zhou,* Bin Fei, Baigang An, Ruimin Sun, Shougen Yin,* and Zunfeng Liu**

Flexible wearable strain sensors have received extensive attention in human–computer interaction, soft robotics, and human health monitoring. Despite significant efforts in developing stretchable electronic materials and structures, developing flexible strain sensors with stable interfaces and low hysteresis remains a challenge. Herein, $Ti_3C_2T_x$ MXene/AgNWs/liquid metal strain sensors (MAL strain sensor) with self-healing function are developed by exploiting the strong interactions between $Ti_3C_2T_x$ MXene/AgNWs/LM and the disulfide and hydrogen bonds inside the self-healing poly(dimethylsiloxane) elastomers. AgNWs lap the $Ti_3C_2T_x$ MXene sheets, and the LM acts as a bridge to increase the lap between $Ti_3C_2T_x$ MXene and AgNWs, thereby improving the interface interaction between them and reducing hysteresis. The MAL strain sensor can simultaneously achieve high sensitivity (gauge factor for up to 3.22), high linearity ($R^2 = 0.98157$), a wide range of detection (e.g., 1%–300%), a fast response time (145 ms), excellent repeatability, and stability.In addition, the MAL strain sensor before and after self-healing is combined with a small fish and an electrothermally driven soft robot, respectively, allowing real-time monitoring of the swinging tail of the small fish and the crawling of the soft robot by resistance changes.

1. Introduction

Resistive strain sensors have attracted the attention of many researchers due to their high sensitivity, simple structure, low cost, good flexibility, ductility, and wearable functionality.[1] Directly compositing a conductive material and a flexible substrate is a comprehensible method to fabricate resistive strain sensors. However, the linear range of the strain sensor made in this way is limited and when the strain exceeds the linear range, the resistance changes erratically. Besides, the relative position of the conductive material in the strain sensor will change greatly during multiple stretch–release processes, resulting in a serious hysteresis problem. Buckled structures have been applied to wearable electronics by many researchers for their ability to improve stretchability and linearity,[2] including hierarchically buckled strain sensor,[3] hierarchically buckled

---

Y. Wang, W. Qin, M. Yang, Z. Tian, S. Yin
School of Materials Science and Engineering
Key Laboratory of Display Materials and Photoelectric Devices
Ministry of Education and Tianjin Key Laboratory for Photoelectric Materials and Devices
Tianjin University of Technology
Tianjin 300384, China
E-mail: wangyanli@stud.tjut.edu.cn; wjqin@tjut.edu.cn; yangmin@stud.tjut.edu.cn; tzh@stud.tjut.edu.cn; sgyin@tjut.edu.cn

Y. Wang, W. Guo, J. Sun, X. Zhou, Z. Liu
State Key Laboratory of Medicinal Chemical Biology
College of Pharmacy and College of Chemistry
Key Laboratory of Functional Polymer Materials
Frontiers Science Center for New Organic Matter
Nankai University
Tianjin 300071, China
E-mail: 9820200114@nankai.edu.cn; sunjinkun@mail.nankai.edu.cn; zhouxiang@cpu.edu.com; liuzunfeng@nankai.edu.cn

X. Zhou
Department of Science
China Pharmaceutical University
Nanjing 211198, China

B. Fei
Institute of Textiles and Clothing
The Hong Kong Polytechnic University
Hong Kong 999077, China
E-mail: bin.fei@polyu.edu.hk

B. An
School of Chemical Engineering
University of Science and Technology Liaoning
Anshan 114051, China
E-mail: bgan@ustl.edu.cn

R. Sun
Research Center of Functional Materials
Kaifeng University
Kaifeng, Henan 475004, China
E-mail: srm@kfu.edu.cn

The ORCID identification number(s) for the author(s) of this article can be found under https://doi.org/10.1002/adfm.202301587

DOI: 10.1002/adfm.202301587

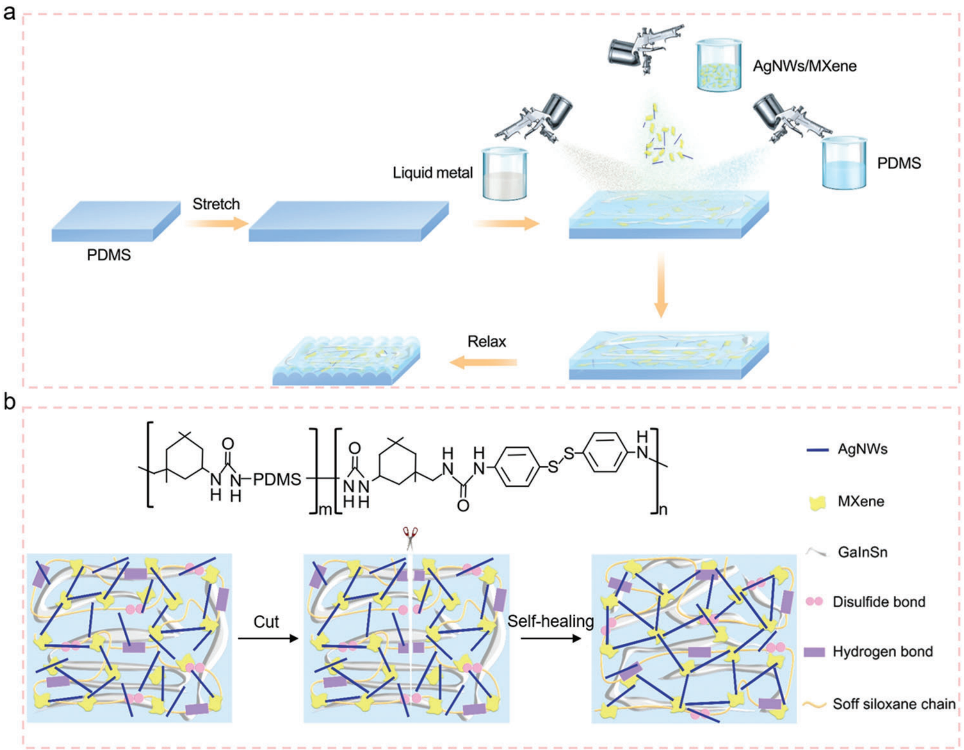

Figure 1. Schematic illustration of MAL flexible strain sensors. a) Different steps illustrated the fabrication of the MAL strain sensor. b) Schematic diagram of the structure change of the MAL strain sensor in the original, cut, and self-healing states.

bisheath strain sensor,[4] sheath–core fiber-based ultrastretchable buckled strain sensor,[5] etc. The introduction of the buckled structure ensured that the strain sensor had good stretchability and linearity while avoiding damage to the strain sensor during stretching, and ensuring the stable performance of the strain sensor. However, it still cannot solve the hysteresis problem caused by the interface compound difference.

Liquid metal (LM) consists of low melting point eutectic gallium–indium–tin (GaInSn), with high electrical conductivity, good fluidity, and large deformability in the liquid state, stable overall conductivity changes under deformation, and negligible hysteresis.[6] We summarized the research work on liquid-metal-based strain sensors (Table S1, Supporting Information),[7] and it can be seen that liquid-metal-based strain sensors have highly stretchability, high linearity, and high sensitivity. Using liquid metal to construct a composite structure can construct a more stable interface, and maintain lower resistance, which is expected to solve the hysteresis problem.

In this work, we developed a $Ti_3C_2T_x$ MXene/AgNWs/LM strain sensor (MAL strain sensor) with a self-healing function by exploiting the strong interaction between $Ti_3C_2T_x$ MXene/AgNWs/LM and disulfide and hydrogen bonds inside the self-healing poly(dimethylsiloxane) (PDMS) elastomer. In this process, AgNWs lapped the $Ti_3C_2T_x$ MXene sheets between each other. The LM acted as a bridge to increase the lap between $Ti_3C_2T_x$ MXene and AgNWs, improving the interface interaction between them and reducing hysteresis. In addition, the buckled structure was introduced to further increase the stretchability and linear range of the strain sensor. The fabricated MAL strain sensor can simultaneously achieve high sensitivity (gauge factor for up to 3.22), high linearity ($R^2 = 0.98157$), a wide range of detection (e.g., 1%–300%), a fast response time (145 ms), excellent repeatability, and stability. The self-healing strain sensor can still accurately capture a variety of human activities, such as large limb movements, small physiological activities, and underwater applications. Further, we applied MAL strain sensor before and after self-healing to an electrothermally driven soft robot to monitor the soft robot's work in real time by the change of resistance.

2. Result and Discussion

2.1. Self-Healing Strain Sensor with Buckled Structure

Figure 1a illustrates the fabrication process of the MAL strain sensor with buckle structure. First, PDMS with a self-healing function was synthesized (see subsection "Synthesis—Synthesis of Self-Healing Elastomer PDMS" in the Experimental Section for details), then the synthesized self-healing PDMS was stretched with 100% prestretching. LM was well soaked with hydrochloric acid (to remove the oxides on the liquid metal surface) (Figure S1, Supporting Information). Directly mixing the $Ti_3C_2T_x$ MXene/AgNWs, LM, and PDMS does not form a uniform solution, instead serious precipitation and phase separation were observed. Therefore, they were sprayed from three separate spray guns, and it was found that relatively uniform network in the final composite sensing layer was obtained by this spray-mixing strategy. The self-healing PDMS can be dissolved in tetrahydrofuran (THF), so the viscosity of the solution can be delicately tuned by controlling the PDMS concentration. We found that the self-healing PDMS solution exhibited significant shear thinning properties at a concentration ranging from 15% to 34% (Figure S2, Supporting Information). Therefore, at a high enough flow rate, the self-healing PDMS solution exhibited shear thinning properties and did not block the nozzle. This was different from the PDMS 184, which was a 3D cross-linking structure and cannot be dissolved in THF. The purpose of spraying self-healing PDMS and conductive materials together was to enable the liquid metal to adhere well to the PDMS substrate and prevent peeling. After drying, the prestretch was released, and then the buckled structure was obtained. Figure S3 (Supporting Information) shows an uncovered LM strain sensor, where the LM conductive layer on the surface was easily wiped off after a light touch of a finger. Figure 1b shows the self-repairing mechanism of the $Ti_3C_2T_x$ MXene/AgNWs/LM in the self-healing PDMS. The mechanism is as follows. Commonly the 1D AgNWs lapping to the 2D MXene form a physical contact, which may separate during straining of the composite and would not recover the initial state because of the small contact area and low interaction force. The existence of the LM between the AgNWs and the $Ti_3C_2T_x$ MXene would serve as the glue to increase the contact area to enhance the interaction. As expected, we observed decreased hysteresis of the $Ti_3C_2T_x$ MXene/AgNW/LM strain sensor than for the $Ti_3C_2T_x$ MXene/AgNW strain sensor. In addition, the self-healing PDMS contains a lot of dynamic bonds (the S–S bond and the multiple hydrogen bonds), which further interact with the AgNWs, $Ti_3C_2T_x$ MXene, and LM via metal–S, and metal–H interactions.

2.2. Strain Sensing and Its Mechanism

First, $\Delta R/R_0$ of MAL strain sensors with and without buckled structures was investigated (**Figure 2**a). For one sample, we obtained very good cycling properties during repeated testing. Therefore, we employed one sample and test the percent resistance change–strain curves for 10 cycles of tests. It was found that the MAL strain sensor without a buckled structure had a relatively high gauge factor with a large variation of $\Delta R/R_0$ in the strain range of 0%–100%, but had a large hysteresis and poor linearity. By contrast, the MAL strain sensors with buckled structures had little hysteresis and high linearity ($R^2 = 0.98157$) in the strain range of 0%–100%. In addition, the effect of different prestretchings of self-healing PDMS flexible substrates on the variation of $\Delta R/R_0$ was investigated. Figure 2b demonstrates that the strain sensors obtained by prestretching to 20%, 40%, 60%, 80%, 100%, 120%, and 140% can be stretched to a maximum of 20%, 40%, 60%, 80%, 100%, 120%, and 140%, respectively, consistent with the prestretching degree. It was found that when the prestretch was less than 100%, $\Delta R/R_0$ increased with the increase of prestretch, and when the prestretch was 100%, it can be seen that obvious cracking was observed at 120% strain for this sample, where the disconnection of the conducting pathway would result in a large increment of $\Delta R/R_0$ (Figure S4, Supporting Information). Therefore, we chose 100% prestretch as the optimal prestretch for the MAL strain sensor. Of course, there were ways to enhance the stretchability of the sensor with stable electrical properties, and the maximum stretchability of the self-healing PDMS elastomer can be adjusted by varying the amounts of isophorone diisocyanate (IPDI) substance during the synthesis process. As shown in Figure S5a (Supporting Information), we increased the stretchability of the self-healing PDMS by reducing the feed ratio of IPDI (rigid segment) during the polymerization process. The maximal available strain range of the self-healing PDMS increased from 100% to 311% as the content of the molar ratio of IPDI to 4-aminophenyl disulfide (AFD) decreased from 2.8 to 2.25. As a result, the strain range of the obtained strain sensor increased to 300% for a prestrain of 300% by employing the obtained sample, which exhibited good linearity, low hysteresis, and $\Delta R/R_0$ (Figure S5b, Supporting Information). Figure S5c (Supporting Information) shows the stress–strain curve of the MAL strain sensor, and it can be seen that the maximum stretchable of the MAL strain sensor was 440%. Figure 2c,d shows the effect of change in the proportion of conductive materials on flexible strain sensors. When the conductive materials in the strain sensor contained only LM, there was no significant hysteresis but the response of $\Delta R/R_0$ was small. When the conductive materials in the strain sensor contained $Ti_3C_2T_x$ MXene/AgNWs, there was significant hysteresis but the response of $\Delta R/R_0$ was large. When $Ti_3C_2T_x$ MXene with 0.1, 0.5, and 1 wt% content was added to the strain sensor, respectively, the $\Delta R/R_0$ increased and there was no significant hysteresis. It can be concluded that $Ti_3C_2T_x$ MXene and AgNWs can improve the sensitivity of the strain sensor, and LM can reduce the hysteresis of the strain sensor. The $\Delta R/R_0$ of the strain sensor was the maximum when the content of $Ti_3C_2T_x$ MXene was 0.5 wt%. Figure 2e shows the effect of the different numbers of conductive layers on the MAL strain sensor. It can be seen that as the number of $Ti_3C_2T_x$ MXene/AgNW/LM layers increased from 10 to 40, the $\Delta R/R_0$ of the strain sensor first increased and then decreased. We studied different numbers of layers including 20, 22, 24, 26, 28, 30, 32, 34, 36, 38, and 40. The $\Delta R/R_0$ of the strain sensor at 100% strain increased from 3.13 to a maximum value of 3.52 as the number of layers increased from 20 to 30 (Figure S6a, Supporting Information), and then decreased to 3.39 as the number of layers further increased to 40 (Figure S6b, Supporting Information). Figure S7a,b (Supporting Information) shows the resistance and scanning electron microscopy (SEM) image of the MAL strain sensor with the number of conductive layers of 6. It can be seen that $Ti_3C_2T_x$ MXene and AgNWs did not form a good lap between each other, so a good conductive path was not achieved. Conversely, since $Ti_3C_2T_x$ MXene/AgNWs were ethanol dispersions, spraying more than 40 layers of $Ti_3C_2T_x$ MXene/AgNW solution on the prestretched 100% MAL strain sensor tended to cause damage to the conductive layer, and cracks can be seen on the surface of the MAL strain sensor from its SEM image after release prestretching (Figure S8, Supporting Information). Compared to the literature, this MAL strain sensor provided the highest strain to-hysteresis ratio (223.2), i.e., the lowest hysteresis (0.448%) was obtained for the same strain (300%) for sensing (Figure 2f). This was important for the strain sensor to be able to detect accurate values in real time.

Figure 3a–f shows the SEM images of the MAL strain sensor with varying prestretchings, when the prestretch increased from 0% to 100%, buckled structures were produced that were perpendicular to the direction of stretching and closely aligned. This buckling structure ensured the extensibility of the material. The

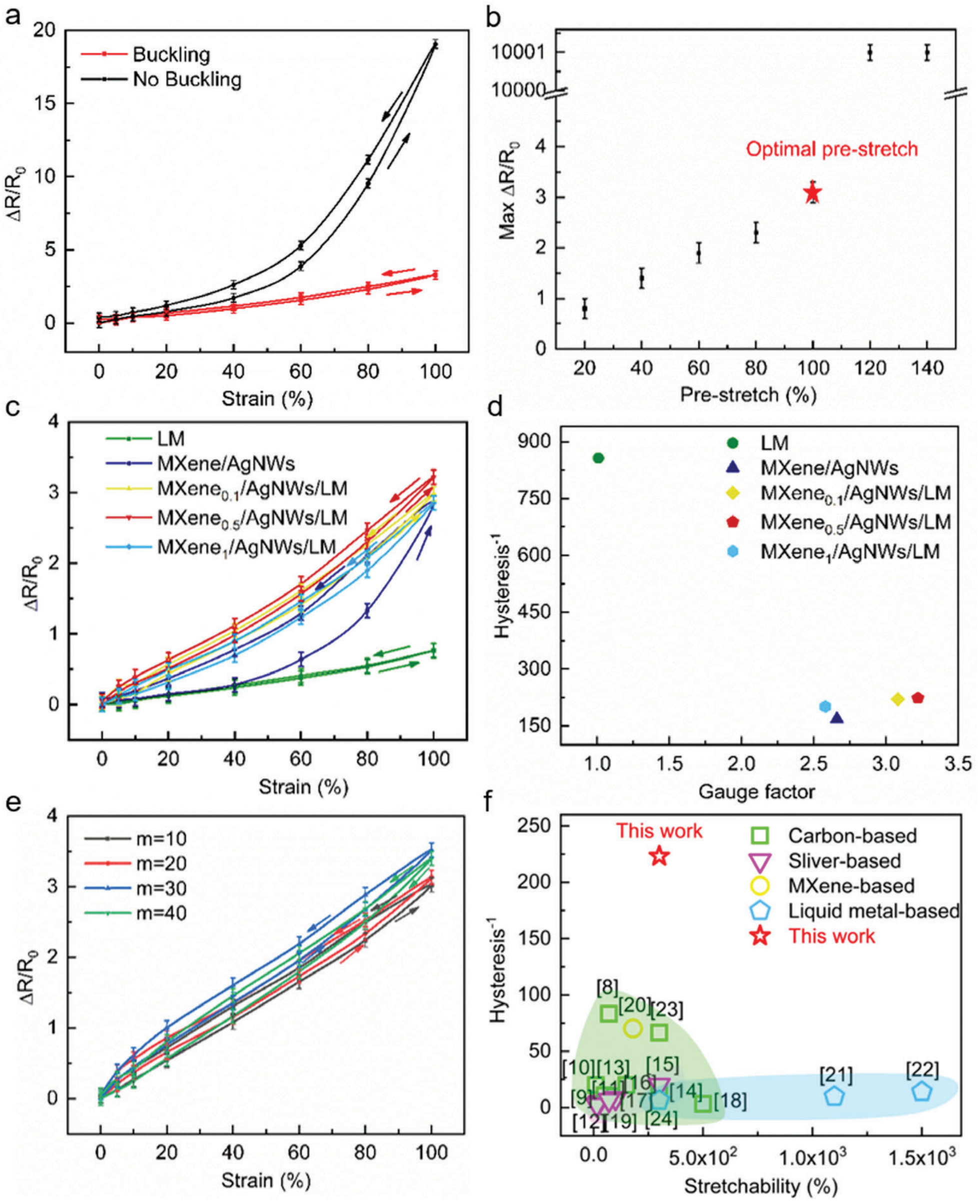

Figure 2. $\Delta R/R_0$ as a function of applied strain for MAL strain sensor: a) with or without buckling structures; b) with varying prestretch values of 20%, 40%, 60%, 80%, 100%, 120%, and 140%, where the red star points toward the optimal prestretching percentage in the subsequent experiments; c) with varying conductive materials. d) Comparison of the gauge factor and hysteresis of the MXene/AgNWs, LM, and MXene/AgNWs/LM strain sensors. e) $\Delta R/R_0$ as a function of applied strain for MAL strain sensor with varying numbers of conductive layers. f) Literature comparison on stretchability and hysteresis of strain sensors in recent years.[8–24]

SEM images of the MAL strain sensor (Figure 3g,h) show that the AgNWs lapped the $Ti_3C_2T_x$ MXene sheets between the layers and the LM acted as a bridge to increase the connection between the $Ti_3C_2T_x$ MXene and AgNWs. The cross-section SEM image of the self-healing strain sensor with buckled structure can be seen in Figure 3i. The energy dispersive spectrometer (EDS) mapping on the cross-section was performed to determine the uniform distribution of C, Ti, Ag, Ga, In, and Sn elements in a conductive elastomer. Thus, it can be seen that the individual conductive materials were evenly distributed in the flexible self-healing PDMS substrate.

2.3. Sensing Characteristics

To evaluate the response time of the MAL strain sensor, a 5% strain at a speed of 400 mm s^{-1} was applied. **Figure 4**a shows that the MAL strain sensor had a response time of 145 ms. We further evaluate the effect of the response speed of the MAL strain sensor on the change in strain velocity. The MAL strain sensor was to 5% at different stretch rates of 1, 3, 5, 10, 200, 400, and 600 mm s^{-1} (Figure 4b), from which it can be seen that the response of the MAL strain sensor was faster as the strain rate increased, and the sensor still exhibited a synchronized response

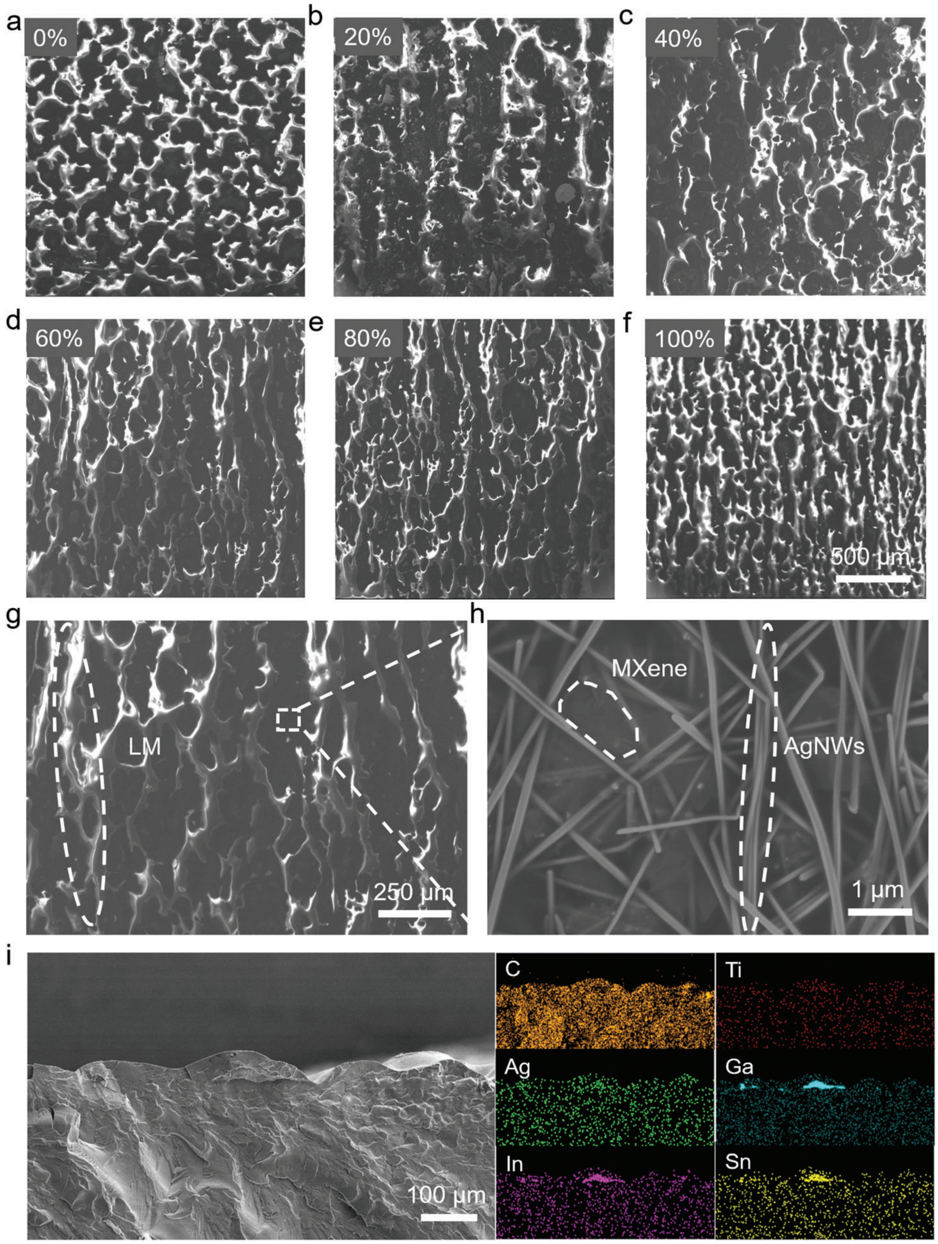

Figure 3. SEM images under different prestretchings: a) 0%, b) 20%, c) 40%, d) 60%, e) 80%, and f) 100%. g,h) Surface SEM images of MAL strain sensor. i) SEM and elemental mapping of its cross-section.

when the strain rate reached 600 mm s^{-1}. The sensitivity of the sensor was determined by evaluating $\Delta R/R_0$ at different strains. As can be seen from Figure 4c, the sensitivity was 3.22 and the linearity was 0.98157 at a strain range of 0–100%, showing good response characteristics. In addition, the samples were subjected to repeated tensile tests at different tensile magnifications of 1%–100%. Figure 4d shows a typical curve of the resistance response, showing the reliability and stability of the MAL strain sensor. Very clear strain triangle characteristics were observed even when the tensile strain was as low as 1%, which meant that the minimum detection can be as low as 1%. Figure 4e shows the variation of $\Delta R/R_0$ for the MAL strain sensor at different strains in the range of 0% to100% with 5 tensile release cycles. The peak value of $\Delta R/R_0$ did not change significantly. The cycling stability remained good when the tensile strain was increased to 100%. Durability was critical in applications that ensure long-term recycling. The stability of the sensor was determined by performing 1000 tensile tests at 10% tensile strain, and the results showed that the MAL strain sensor had good cyclic stability (Figure 4f).

To highlight the good interface stability between the self-healing PDMS and the conductive layer, we compared the self-healing PDMS with the non-self-healing PDMS 184 strain

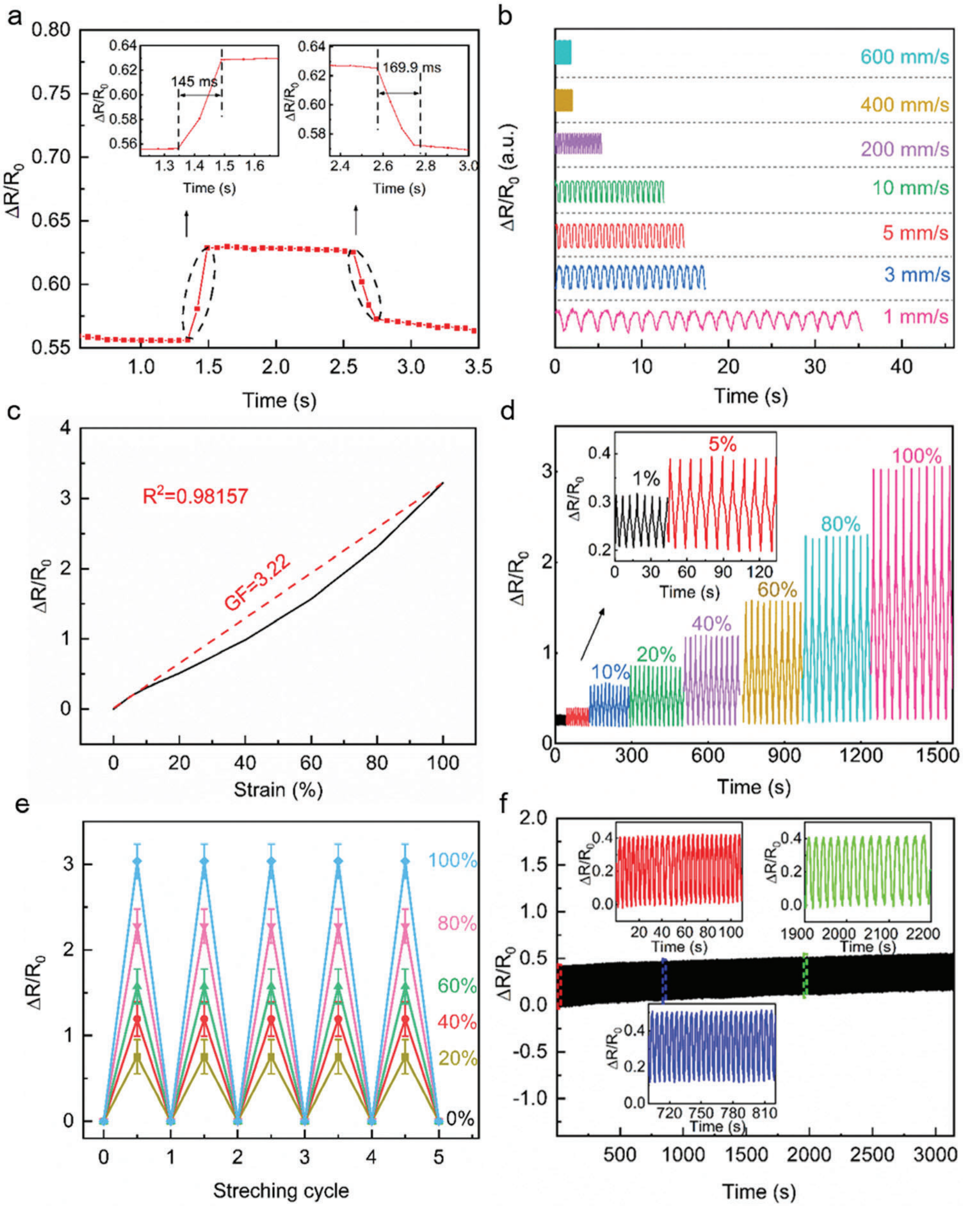

Figure 4. Characterization of MAL strain sensor. a) Strain sensor response time and recovery time at 5% strain and 400 mm s^{-1} tensile speed rate. b) $\Delta R/R_0$ of response speed for different stretching speeds stretched to 5% of MAL strain sensors. c) In the range of 0%–100% strain, the percentages of changes in the resistances and gauge factors correspond to different stretch strains. d) $\Delta R/R_0$ of the MAL strain sensor when the strain was increased from 1% to 100%. e) $\Delta R/R_0$ at different stretching/release cycles of the MAL strain sensor. f) When the stretching strain was 10% with 1000 strain cycles.

sensor. It was found that the $\Delta R/R_0$ change of the self-healing strain sensor was higher, and the hysteresis of the self-healing strain sensor was significantly smaller than that of the PDMS 184 strain sensor when stretched within 100% (Figure S9a, Supporting Information). Figure S10a (Supporting Information) demonstrates the response time of the PDMS 184 sensor stretched to 5% strain sensor at the speed of 400 mm s^{-1}, its response time reached 219.1 ms, higher than the MAL strain sensor. The PDMS 184 strain sensor was nonlinear with a sensitivity of 0.18 over the strain range of 0–80% and 1.64 over the strain range of 80–100% (Figure S10b, Supporting Information). Figure S10c (Supporting Information) shows that the PDMS 184 strain sensor had poor cycle stability during 1000 tensile release cycles. The contact angle test (Figure S9b,c, Supporting Information) shows that self-healing PDMS had a contact angle of 40.6° with liquid metal and PDMS 184 had a contact angle of 109.7° with liquid metal, so self-healing PDMS had a stronger affinity with liquid metal and has better adhesion. Therefore, when the composite effect between LM and self-healing PDMS substrate was better than that between LM and PDMS 184 substrate, a stable interface between LM and self-healing PDMS can be maintained during multiple stretch–release processes. On the contrary, the poor contact interface between LM and PDMS 184 during multiple tensile releases tended to cause the

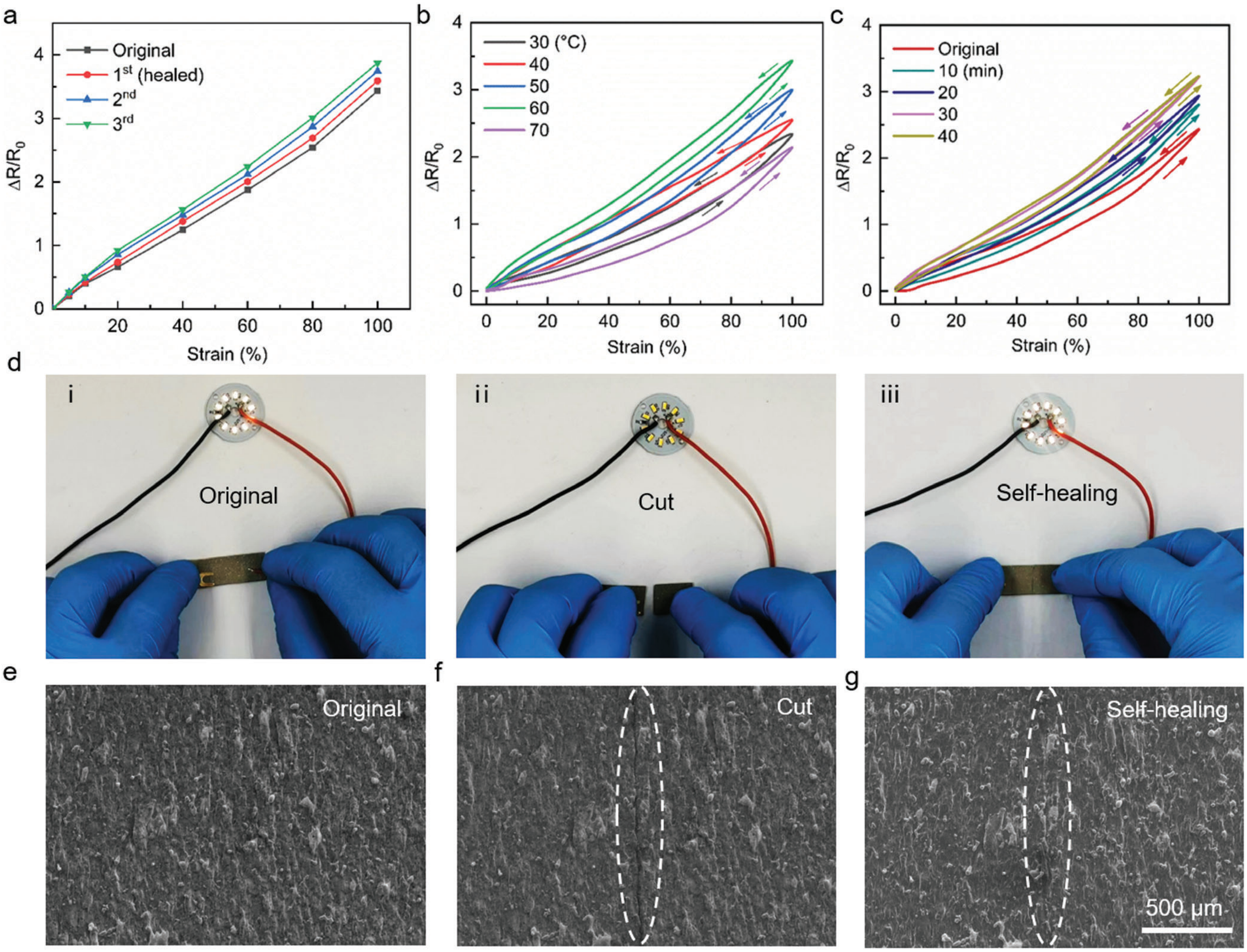

Figure 5. a) $\Delta R/R_0$ as a function of applied strain for the MAL strain sensor with varying healing times of initial, first, second, and third times. b) $\Delta R/R_0$ as a function of applied strain for the MAL strain sensor with varying healing temperatures. c) $\Delta R/R_0$ as a function of applied strain for the MAL strain sensor with varying healing times. d) When the MAL strain sensor was connected to a LED lamp, the LED lamp was light and dark in the i) original, ii) cutting, and iii) self-healing states, respectively. e–g) SEM images of the MAL strain sensor in its (e) original, (f) cut, (g) after self-healing states.

relative position movement between LM and PDMS 184 substrate, resulting in a larger response of $\Delta R/R_0$ and poorer cyclic stability.

2.4. Self-Healing Properties of MAL Strain Sensor

Figure 5a shows the variation curves of $\Delta R/R_0$ with the tensile strain for the MAL strain sensor in the original state and after the first, second, and third self-healing processes. It can be seen that the $\Delta R/R_0$ increased from the original state to the third self-healing of the MAL strain sensor. We investigated 10 fully cutting and self-healing cycles, the MAL strain sensor still exhibited good linearity, and the $\Delta R/R_0$ at 100% strain increased from 3.43 to 4.68 for 10 cutting–healing cycles (Figure S11, Supporting Information). Then, we investigated the effects of temperature and time of the self-healing process on the performance of the strain sensor. The results showed that the $\Delta R/R_0$ of the strain sensor first increased and then decreased when the healing temperature increased from 30 to 70 °C, and the value of $\Delta R/R_0$ was the maximum when the self-healing temperature was 60 °C (Figure 5b). Besides, when the self-healing time increased from 10 to 40 min, the $\Delta R/R_0$ of the strain sensor gradually increased, and when the self-healing time reached 30 and 40 min, their $\Delta R/R_0$ curves almost coincided, so the optimal self-healing time of the MAL strain sensor was 30 min (Figure 5c).

In addition, we connected the self-healing elastic conductor to a light emitting diode (LED) lamp. The elastic conductor in the original state remained intact and the LED lamp stayed on when connected to the lamp (Figure 5d-i). When the MAL strain sensor was cut, the LED turned off (Figure 5d-ii). After self-healing at 60 °C for 30 min, the LED lamp lit up again, indicating that the conductive path of the MAL strain sensor was restored (Figure 5d-iii). Figure 5e-g shows the SEM images of the MAL elastic conductor in original, cut, and after self-healing, respectively.

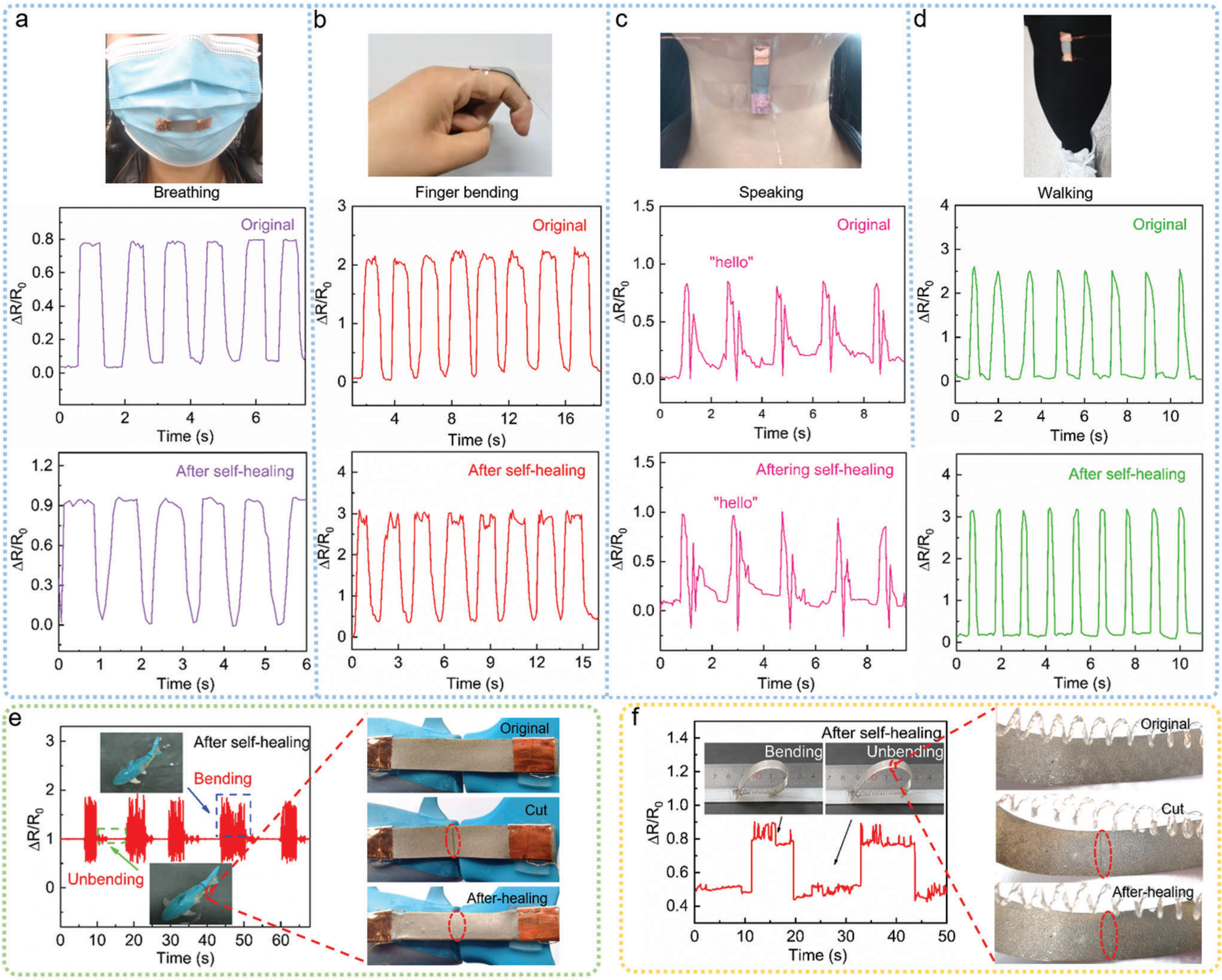

Figure 6. Application of strain sensor before and after self-healing in human motion monitoring: a) monitoring of breathing, b) monitoring of finger bending, c) monitoring of speaking, and d) monitoring of walking. e) MAL strain sensors adhered to the tail to monitor the tail swing: original and after self-healing. Photographs of MAL strain sensor installed on the tail of a robot fish for the original, cut, and self-healing samples. f) Photographs of the MAL strain sensor installed on the soft crawling robot for the original, cut, and self-healing samples.

2.5. Applications of MAL Strain Sensor

The MAL strain sensor was fixed on the human muscle or joint with tape, and the deformation caused by human activities (such as breathing, finger bending, speaking, and walking) was monitored in real time (**Figure 6**a–d).

By mounting the MAL strain sensor to the body of a small fish, it was able to monitor the tail oscillation of the fish swimming in the water in real time (Figure S12a, Supporting Information). When the sensor was cut and then self-healed at room temperature for 12 h, the MAL strain sensor can still realize underwater monitoring. Figure 6e shows the MAL strain sensor capable of monitoring the tail oscillation of fish swimming in water in real time and the photographs of the MAL strain sensor in its original state, cut-off state, and after self-healing, respectively.

We combined MAL strain sensors with electrothermally driven soft robots to realize that the MAL strain sensor can monitor the crawling of soft robots in real time. First, a certain length of nylon 6 fish wire with a diameter of 0.4 mm and copper wire with a diameter of 0.05 mm were fixed on the stepper motor at one end, and the other end was suspended with a 5 g weight and set on a crank pin, twisted at a twisting density of 6.25 turns cm^{-1}, and heterochiral rod winding, and annealed in a vacuum drying oven at 120 °C and 120 min, and finally removed from the vacuum drying oven. The artificial muscle fibers were prepared with the function of heat shrinkage and cold expansion. In addition, a polyethylene terephthalate (PET) film was used as a skeleton for the crawling of the soft robot, and a MAL strain sensor was prepared on the PET film with a thickness of 0.2 mm. The artificial muscles were fixed to the two ends of the PET film. Finally, we obtained the soft crawling robot with the composite MAL strain sensor. The artificial fiber muscles wound by thin copper wires were able to contract under 2 W electrical power, which drove the soft robot to crawl forward. The sensor layer was fully cut and self-healed at room temperature for 12 h. It works well for sensing the walking of the crawling robot (Figure S12b, Supporting Information). The MAL strain sensor enables the crawling robot self-sensing capacity with high linearity, low hysteresis, reasonable sensitivity, and self-healing capacity. Figure 6f shows photographs of the MAL strain sensor capable of monitoring the crawling of the soft robot in real time and the MAL strain sensor in its original state, cut-off state, and after self-healing, respectively.

3. Conclusion

In this study, we developed $Ti_3C_2T_x$ MXene/AgNW/liquid metal strain sensors with a self-healing function by taking advantage of the strong interaction between $Ti_3C_2T_x$ MXene/AgNWs/LM and the disulfide and hydrogen bonds inside the self-healing PDMS elastomer. In the process, AgNWs connected the $Ti_3C_2T_x$ MXene layers. LM acted as a bridge, adding a lap between $Ti_3C_2T_x$ MXene/AgNWs, which improved the interface interaction between them and reduced hysteresis. In addition, the buckled structure further increased the stretchability and linear range of the strain sensor. The fabricated MAL strain sensor displayed high sensitivity (gauge factor (GF) for up to 3.22), high linearity ($R^2 = 0.98157$), a wide range of detection (e.g., 1%–300%), a fast response time (145 ms), excellent repeatability, and stability. In addition, a variety of human activities can be accurately captured by self-healing strain sensors, such as large limb movements and small physiological activities. The repairability of this MAL had also been proven in underwater applications. In addition, by integrating the MAL strain sensor before and after self-healing with an electrothermally driven soft robot, the MAL strain sensor can monitor the operation of the soft robot in real time through the change of resistance during the crawling process of the soft robot. All these excellent properties ensured the operability of the sensor in complex environments. This strain sensor was successfully applied in real time to potential wearable devices that monitor the movements of various humans and robots in real time. We believe that this work will have great potential in biomedicine, such as wearable electronic devices, artificial skin, personal health monitoring and soft robots, and more.

4. Experimental Section

Materials: Bis(3-aminopropyl) terminated poly(dimethylsiloxane)M_n = 3000 and 5000 g mol^{-1}) were purchased from Gelest. AFD (98%), IPDI (99%), and anhydrous THF (99.5%) were purchased from Aladdin (China). LM (GaInSn (gallium (65%)–indium (21.5%)–tin (10%)), melting point: 11 °C, density:6.44 g cm^{-3}) was purchased from Hunan Xineng New Materials Co., Ltd. Titanium aluminum carbide (Ti_3AlC_2, mesh size, 200 µm) was obtained from Jilin 11 Technology Co., Ltd. (Jilin, China). Lithium fluoride (LiF, purity, > 99%), hydrochloric acid (HCl, 35 wt%), and ethanol were purchased from Aladdin Reagent Co., Ltd. (Shanghai, China). AgNWs were purchased from Shanghai Buhan Chemical Technology Co., Ltd. All of the reagents were of analytical grade and used as received without any further purification.

Synthesis—Synthesis of MXene (Ti_3AlC_2) Suspension: MXene ($Ti_3C_2T_x$) was synthesized by etching the Ti_3AlC_2 MAX phase with LiF/HCl mixture solution. Briefly, LiF (mass, 1.6 g) was dissolved in 20 mL of a 9 M HCl solution and mechanically stirred at 400 rotations min^{-1} (rpm) for up to 5 min. Thereafter, Ti_3AlC_2 (mass, 1 g) was added to the above mixture solution and stirred for up to 24 h at 35 °C and 1000 rpm. The obtained dispersion was centrifuged at 3500 rpm for up to 15 min, and the precipitates were ultrasonically washed with deionized water. The washing was continued until the pH of the solution reached more than 6. By this time point, the dark-green precipitates of MXene were evenly dispersed in the water to yield a light-green solution due to the Tyndall effect (Figure S13a, Supporting Information). The structural and morphological analysis of the MXene was carried out by using X-ray diffraction (XRD) (Figure S13b, Supporting Information), SEM (Figure S13c, Supporting Information), and transmission electron microscopy (TEM) (Figure S13d, Supporting Information).

Synthesis—Synthesis of Self-Healing Elastomer PDMS: The elastomer PDMS was prepared by adjusting the molar ratio of P3K (PDMS, M_n = 3000 g mol^{-1}), P5K (PDMS, M_n = 5000 g mol^{-1}), AFD, and IPDI. The preparation method was as follows: P3K5K (P3K, 1.5 g, 0.5 mmol and P5K, 2.5 g, 0.5 mmol) was placed in an oil bath at 100 °C, heated for 30 min to remove impurities from PDMS, and cooled to room temperature. Then, 10 mL of THF was added for dilution, and IPDI (0.373 g, 1.68 mmol) was dissolved into THF (5 mL) and added to the reaction vessel. The reaction was stirred overnight and then heated to 60 °C and stirred for 2 h. AFD (0.15 g, 0.6 mmol) dissolved in THF (10 mL) was then added to the reaction vessel as a chain extender. Until the –NCO peak disappeared in the Fourier transform infrared spectroscopy, PDMS elastomers with self-healing functions were successfully synthesized (Figure S14, Supporting Information). To demonstrate the excellent mechanical properties and flexibility of the self-healing PDMS nanocomposites, Differential scanning calorimetry (DSC) tests were performed that demonstrated the flexibility in PDMS samples with a glass transition temperature (T_g) of –2.5 °C for PDMS (Figure S15, Supporting Information). To demonstrate the complete conversion of diisocyanate groups to carbamate bonds, ^{1}H NMR and Fourier transform infrared spectra (FT-IR) of PDMS elastomers were performed. In the ^{1}H NMR spectrum of PDMS, the peaks of the S–S aromatic unit appeared at 7.42–6.67 ppm, the peaks of PDMS protons appeared at 4.00–1.46 ppm, and the peaks of the IPDI alkyl unit appeared at 0.12–0.06 ppm. The integral ratios of each unit were well-matched with the feed molar ratio (Figure S16, Supporting Information). FT-IR characterization of the preparation process for PDMS elastomers—comparing the FT-IR curves of PDMS elastomers with the monomers, the disappeared peaks of the amide group (–NH_2) at 3370 cm^{-1} and isocyanate group (–NCO) at 2250 cm^{-1} indicated completion of the preparing processes (Figure S14, Supporting Information). The self-healing properties of PDMS elastomers were tested (Figure S17, Supporting Information). Self-healing PDMS could be greatly affected by temperature and time, and the mechanical properties of self-healing elastomer PDMS at the same self-healing temperature at a stretching rate of 20 mm min^{-1} for different self-healing times can be seen in Figure S17a (Supporting Information). The stress intensity was the maximum at 30 min. The mechanical properties of the elastomer PDMS at different stretching rates can be seen in Figure S17b (Supporting Information), where it can be seen that the strain decreased and the stress increased as the stretching rate increased. In the self-healing elastomer, the disulfide units acted as reversible cross-linking points, thus generating elasticity and maintaining the robustness of the polydimethylsiloxane elastomer, while the hydrogen bonding behaved as a weak bond, dissipating strain energy by fracture and reforming at rest. Narrow-amplitude X-ray photoelectron spectroscopy analysis (XPS) scans of the PDMS were performed to characterize the concentration of dynamic disulfide units (Figure S18, Supporting Information). The prepared self-healing PDMS was able to withstand 700% of the tensile strain (Figure S19a, Supporting Information) and was able to stretch again after achieving good self-healing at 60 °C for 30 min (Figure S19b, Supporting Information). In addition, the elastomer was able to lift 200 and 500 g weights before and after self-healing (Figure S19c, Supporting Information).

Preparation of Self-Healing Friction-Resistant Strain Sensor: First, the synthesized PDMS solution was evenly poured into the polytetrafluoroethylene mold with a length of 2 cm and a width of 1.5 cm, and after the solvent evaporated, a PDMS elastomer film with a thickness of 1.5 mm was formed. Next, the PDMS elastomer films were prestretched. Then, ethanol-dispersed $Ti_3C_2T_x$ MXene/AgNWs, liquid metal, and self-healing PDMS were sprayed simultaneously. Finally, a strain sensor with a self-healing buckling structure was obtained after releasing the prestretch. It was important to note that for each sample, the liquid flow rate in the gun, the distance between the gun and the sample, the spraying time were kept the same for each spraying to control the amount of each conductive layer sprayed into the self-healing PDMS substrate. The distance between the gun and the sample was 10 cm for each layer and the spray time was 5 s for each application.

Characterization: For the self-healing properties of PDMS elastomers, the surface chemistry was crucial to determine the molecular chain mobility and dynamic bond exchanges, XPS experiment was conducted to study the surface chemical composition of PDMS using a monochromatic Al Kα radiation (1486.6 eV) and the analysis run at ultrahigh vacuum (2.0109 Torr), and the resultant data were analyzed with the Casa XPS software. DSC was performed on TA Instruments DSC Q20 with a heating rate of 10 °C min^{-1} from −40 to 100 °C. Surface-enhanced Raman spectrum (InVia-Reflex) and FT-IR (Thermos Nicolet 6700 spectrometer) were collected to characterize the surface chemical structure. The electrical properties of the sensor were evaluated by using a two-point probe multimeter (Keithley 2400, Wuhan, China). The reversible strain was measured by IAI electric cylinder high-speed linear slide (rco2-sa6c, Japan). The morphology of the materials and the devices were discerned by SEM (SU8010, Hitachi, Japan) and TEM (JEM-2100F, JEOL). XRD patterns were collected by using XRD (Ultima IV, Rigaku Smart Lab system) using Cu-Kα radiation (λ = 1.54 Å) at a scanning rate of 2θ at 20° min^{-1}. A metallurgical microscope (Chen xing ML 1000, Shanghai, China) was employed for optical imaging. A 0.05 μm diameter copper wire and a 430 μm diameter nylon 6 fishing line fiber (Coats and Clark Co., Ltd.) were twisted together using a servomotor (42-step, Huatian Technology Co., Ltd.). Unless otherwise specified, all of the stresses and strains were expressed engineering values.

Definition of Sensitivity and Hysteresis: The sensitivity of the sensor was determined by assessing relative resistances under different stretching strains. It was defined as follows: $GF = ((R - R_0)/R_0)/\varepsilon$, where ε was the stretching strain, R_0 was the initial resistance, and R was the resistance when stretched to different strains.

The baseline increase in $\Delta R/R_0$ indicated a typical hysteresis pattern. The degree of hysteresis (DH) was calculated to compare the hysteresis performance among various sensors

$$DH = \frac{A_{\text{loading}} - A_{\text{unloading}}}{A_{\text{loading}}} \times 100\% \tag{1}$$

where A_{loading} and $A_{\text{unloading}}$ were the areas of the loading and unloading curves, respectively. A lower value of DH meant less delay in the electrical response.[25] The hysteresis was due mainly to the friction between the filler elements and matrix, which in turn was due to the slippage of fillers under stretching and the delay time associated with re-establishing the percolation network upon releases.[26]

Supporting Information

Supporting Information is available from the Wiley Online Library or from the author.

Acknowledgements

This work was supported by the National Key Research and Development Program of China (Grant Nos. 2019YFE0119600, 2022YFB3807103), the National Natural Science Foundation of China (Grant Nos. 52090034, 52225306, 51973093, and 51773094), the Frontiers Science Center for New Organic Matter, Nankai University (Grant No. 63181206), the National Special Support Plan for High-Level Talents People (Grant No. C041800902), the Science Foundation for Distinguished Young Scholars of Tianjin (Grant No. 18JCJQJC46600), the Fundamental Research Funds for the Central Universities (Grant No. 63171219), the Operation Huiyan (Grant No. 62502510601), the Henan provincial science and technology research project (Grant No. 222102210154), and the Kaifeng Science and Technology Project (industrial areas) (Grant No. 2201004). Informed written consent from all human participants was obtained prior to the research.

Conflict of Interest

The authors declare no conflict of interest.

Data Availability Statement

The data that support the findings of this study are available from the corresponding author upon reasonable request.

Keywords

artificial muscles, buckled structures, liquid metals, low hysteresis, self-healing, soft robotics, $Ti_3C_2T_x$ MXene

Received: February 10, 2023
Revised: April 29, 2023
Published online: May 28, 2023

---

[1] a) B. W. An, K. Kim, H. Lee, S. Y. Kim, Y. Shim, D. Y. Lee, J. Y. Song, J. U. Park, *Adv. Mater.* **2015**, *27*, 4322; b) Y. Y. Chen, Y. Sun, Q. B. Zhu, B. W. Wang, X. Yan, S. Qiu, Q. W. Li, P. X. Hou, C. Liu, D. M. Sun, H. M. Cheng, *Adv. Sci.* **2018**, *5*, 1700965; c) Y. Z. Chen, C. Wang, Z. Y. Wu, Y. Xiong, Q. Xu, S. H. Yu, H. L. Jiang, *Adv. Mater.* **2015**, *27*, 5010; d) Y. Duan, Y. Huang, Z. Yin, N. Bu, W. Dong, *Nanoscale* **2014**, *6*, 3289; e) T. He, C. Lin, L. Shi, R. Wang, J. Sun, *ACS Appl. Mater. Interfaces* **2018**, *10*, 9653; f) Y. Joo, J. Byun, N. Seong, J. Ha, H. Kim, S. Kim, T. Kim, H. Im, D. Kim, Y. Hong, *Nanoscale* **2015**, *7*, 6208; g) J. Lee, K. An, P. Won, Y. Ka, H. Hwang, H. Moon, Y. Kwon, S. Hong, C. Kim, C. Lee, S. H. Ko, *Nanoscale* **2017**, *9*, 1978; h) H. Li, Z. Tan, L. Yuan, J. Li, X. Chen, D. Ji, K. Zhang, W. Hu, L. Li, *Sci. China Mater.* **2020**, *64*, 717; i) C. Luo, J. Jia, Y. Gong, Z. Wang, Q. Fu, C. Pan, *ACS Appl. Mater. Interfaces* **2017**, *9*, 19955; j) F. Sun, M. Tian, X. Sun, T. Xu, X. Liu, S. Zhu, X. Zhang, L. Qu, *Nano Lett.* **2019**, *19*, 6592; k) W. Wang, L. Lu, Z. Li, L. Lin, Z. Liang, X. Lu, Y. Xie, *ACS Appl. Mater. Interfaces* **2022**, *14*, 1315; l) L. Sun, H. Huang, Q. Ding, Y. Guo, W. Sun, Z. Wu, M. Qin, Q. Guan, Z. You, *Adv. Fiber Mater.* **2021**, *4*, 98; m) R. Xu, M. She, J. Liu, S. Zhao, H. Liu, L. Qu, M. Tian, *Adv. Fiber Mater.* **2022**, *4*, 1525; n) J. Zhang, Y. Liu, J. Li, H. Zhou, J. Ma, A. Li, Y. Wang, H. Zhu, D. Han, Y. Zhang, *IEEE Photonics Technol. Lett.* **2022**, *34*, 1361; o) R. You, Y. Q. Liu, Y. L. Hao, D. D. Han, Y. L. Zhang, Z. You, *Adv. Mater.* **2020**, *32*, 1901981; p) R. You, D.-D. Han, F. Liu, Y.-L. Zhang, G. Lu, *Sens. Actuators, B* **2018**, *277*, 114; q) J. N. Ma, Y. L. Zhang, Y. Q. Liu, D. D. Han, J. W. Mao, J. R. Zhang, W. C. Zhao, H. B. Sun, *Kexue Tongbao (Foreign Lang. Ed.)* **2022**, *67*, 501; r) L.-N. Fang, J.-C. Li, J.-R. Zhang, D.-D. Han, *IEEE Photonics J.* **2021**, *13*, 1.
[2] a) T. R. Hendricks, W. Wang, I. Lee, *Soft Matter* **2010**, *6*, 3701. b) J. B. Kim, P. Kim, N. C. Pégard, S. J. Oh, C. R. Kagan, J. W. Fleischer, H. A. Stone, Y.-L. Loo, *Nat. Photonics* **2012**, *6*, 327; c) C. Yang, L. Li, J. Zhao, J. Wang, J. Xie, Y. Cao, M. Xue, C. Lu, *ACS Appl. Mater. Interfaces* **2018**, *10*, 25811; d) J. Sun, X. Pu, M. Liu, A. Yu, C. Du, J. Zhai, W. Hu, Z. L. Wang, *ACS Nano* **2018**, *12*, 6147; e) Z. Zhang, C. Xie, J. Zhang, M. Chan, M. Zhang, *Carbon* **2022**, *197*, 218.
[3] Y. Wang, W. Qin, X. Hu, Z. Liu, Z. Ren, H. Cao, B. An, X. Zhou, M. Shafiq, S. Yin, Z. Liu, *Sens. Actuators, B* **2022**, *368*, 132228.
[4] R. Wang, N. Jiang, J. Su, Q. Yin, Y. Zhang, Z. Liu, H. Lin, F. A. Moura, N. Yuan, S. Roth, R. S. Rome, R. Ovalle-Robles, K. Inoue, S. Yin, S.

Fang, W. Wang, J. Ding, L. Shi, R. H. Baughman, Z. Liu, *Adv. Funct. Mater.* **2017**, *27*, 1702134.
[5] L. Li, H. Xiang, Y. Xiong, H. Zhao, Y. Bai, S. Wang, F. Sun, M. Hao, L. Liu, T. Li, Z. Peng, J. Xu, T. Zhang, *Adv. Sci.* **2018**, *5*, 1800558.
[6] a) J. Cheng, J. Shang, S. Yang, J. Dou, X. Shi, X. Jiang, *Adv. Funct. Mater.* **2022**, *32*, 2200444; b) C. Zhao, Y. Wang, L. Gao, Y. Xu, Z. Fan, X. Liu, Y. Ni, S. Xuan, H. Deng, X. Gong, *ACS Appl. Mater. Interfaces* **2022**, *14*, 21564; c) J. Chen, J. Zhang, Z. Luo, J. Zhang, L. Li, Y. Su, X. Gao, Y. Li, W. Tang, C. Cao, Q. Liu, L. Wang, H. Li, *ACS Appl. Mater. Interfaces* **2020**, *12*, 22200; d) H. Wang, R. Li, Y. Cao, S. Chen, B. Yuan, X. Zhu, J. Cheng, M. Duan, J. Liu, *Adv. Fiber Mater.* **2022**, *4*, 987.
[7] a) M. Sun, P. Li, H. Qin, N. Liu, H. Ma, Z. Zhang, J. Li, B. Lu, X. Pan, L. Wu, *Chem. Eng. J.* **2023**, *454*, 140459; b) X. Chen, P. Sun, H. Tian, X. Li, C. Wang, J. Duan, Y. Luo, S. Li, X. Chen, J. Shao, *J. Mater. Chem.* **2022**, *10*, 1039; c) H. Guo, X. Lv, W. Chen, Y. Zhang, W. Zou, L. Liu, H. Yu, *Adv. Mater. Technol.* **2023**, *8*, 2200749.
[8] Q. Xia, S. Wang, W. Zhai, C. Shao, L. Xu, D. Yan, N. Yang, K. Dai, C. Liu, C. Shen, *Compos. Commun.* **2021**, *26*, 100809.
[9] J. Lee, S. Kim, J. Lee, D. Yang, B. C. Park, S. Ryu, I. Park, *Nanoscale* **2014**, *6*, 11932.
[10] X. Li, R. Zhang, W. Yu, K. Wang, J. Wei, D. Wu, A. Cao, Z. Li, Y. Cheng, Q. Zheng, R. S. Ruoff, H. Zhu, *Sci. Rep.* **2012**, *2*, 870.
[11] X. Li, T. Hua, B. Xu, *Carbon* **2017**, *118*, 686.
[12] Z. Yang, D. Y. Wang, Y. Pang, Y. X. Li, Q. Wang, T. Y. Zhang, J. B. Wang, X. Liu, Y. Y. Yang, J. M. Jian, M. Q. Jian, Y. Y. Zhang, Y. Yang, T. L. Ren, *ACS Appl. Mater. Interfaces* **2018**, *10*, 3948.
[13] S. Zhang, H. Zhang, G. Yao, F. Liao, M. Gao, Z. Huang, K. Li, Y. Lin, *J. Alloys Compd.* **2015**, *652*, 48.
[14] J. T. Muth, D. M. Vogt, R. L. Truby, Y. Menguc, D. B. Kolesky, R. J. Wood, J. A. Lewis, *Adv. Mater.* **2014**, *26*, 6307.
[15] O. Atalay, W. R. Kennon, *Sensors* **2014**, *14*, 4712.
[16] U.-H. Shin, D.-W. Jeong, S.-M. Park, S.-H. Kim, H. W. Lee, J.-M. Kim, *Carbon* **2014**, *80*, 396.
[17] H. J. Kim, A. Thukral, C. Yu, *ACS Appl. Mater. Interfaces* **2018**, *10*, 5000.
[18] J. Shintake, Y. Piskarev, S. H. Jeong, D. Floreano, *Adv. Mater. Technol.* **2017**, *3*, 1700284.
[19] X. Zheng, Q. Wang, J. Luan, Y. Li, N. Wang, *Micromachines* **2019**, *14*, 300.
[20] G. Jin, Y. Sun, J. Geng, X. Yuan, T. Chen, H. Liu, F. Wang, L. Sun, *Nano Energy* **2021**, *84*, 105896.
[21] X. Wang, N. Li, J. Yin, X. Wang, L. Xu, T. Jiao, Z. Qin, *Sci. China Mater.* **2022**, *66*, 272.
[22] G. Xue, Y. Shi, S. Wang, H. Zhou, Z. Chen, W. Guo, Y. Yang, M. Ye, *Chem. Eng. J.* **2023**, *456*, 140976.
[23] L. Wang, Z. Zhang, J. Cao, W. Zheng, Q. Zhao, W. Chen, X. Xu, X. Luo, Q. Liu, X. Liu, J. Xu, B. Lu, *Polymers* **2022**, *15*, 90.
[24] S. Zhang, J. Xu, *Polymers* **2022**, *14*, 5401.
[25] S. G. Yoon, H. J. Koo, S. T. Chang, *ACS Appl. Mater. Interfaces* **2015**, *7*, 27562.
[26] M. Amjadi, K.-U. Kyung, I. Park, M. Sitti, *Adv. Funct. Mater.* **2016**, *26*, 1678.